Publications of the Astronomical Society of the Pacific, **117**:536–543, 2005 May

Optical Turbulence Profiling with Balloons Relevant to Astronomy and Atmospheric Physics

M. Azouit and J. Vernin

Laboratoire Universitaire d'Astrophysique de Nice, UMR 6525, Université de Nice-Sophia, Antipolis F-06108 Nice, Cedex 2, France; azouit@unice.fr, vernin@unice.fr

Received 2004 February 11; accepted 2005 February 21; published 2005 April 26

ABSTRACT. We present here an in situ technique to measure the microstructure of the temperature field in our atmosphere. It consists of an autonomous payload that computes the structure function of the temperature, along with an off-the-shelf meteorological sonde that gives air pressure, temperature, humidity, and wind speed. This technique, which has been intensively cross-calibrated, gives a high spatiotemporal resolution, allowing us to achieve an optical turbulence profile $C_N^2(h)$ with a better than 6 m vertical resolution. It has been designed to allow simultaneous measurements of the temperature structure function in various geometrical configurations. Its versatility, reliability, and accuracy helped us to successfully undertake many astronomical site testing campaigns, as well as offer new insights into the physics of the optical turbulence.

1. INTRODUCTION

Since the 1960s, modern astronomy in the visible range has required quantitative measurements of the optical turbulence strength at different altitudes to improve the seeing at the focus of already existing telescopes and to search for new sites where a new class of instrument (4 m at the beginning and then 8 m and more) could be installed. First, a geographical study was performed to select the best potential areas, and then attention was concentrated on a few sites where intensive investigations were set up, including mast, balloon, and seeing monitors (such as the differential image motion monitor; DIMM), a generalized seeing monitor (GSM), SCIDAR (scintillation detection and ranging), then generalized SCIDAR (GS), and finally meteorological models.

Image motion, blurring, and scintillation are responsible for the majority of loss in angular precision of large, ground-based telescopes, due to phase and amplitude distortion at the entrance pupil. These disturbances occur when the optical beam, unaffected at the top of our atmosphere (≈30 km), reaches the first turbulent layers, which generate refractive index fluctuations, mainly related to the temperature turbulent field, in the visible range. In radio and millimeter astronomy, the refractive index is related to humidity changes (Bean & Dutton 1968).

In the 1970s, with the pioneering works of Bufton et al. (1972), Bufton (1973a, 1973b), Coulman (1972), and Barletti et al. (1976, 1977), the first balloons equipped with microthermal sensors were successfully launched, and now, 40 yr later, improvements have been made, although the principle still remains the same. A typical launch train includes a helium balloon that lifts a payload with which temperatures are measured. These are separated by a long (50 m or more) rope to avoid any turbulent perturbation from the balloon's wake. Since the expected temperature fluctuations are of the order of a mK, a differential technique is applied using two sensors about 1 m apart. Then amplification is made onboard.

With the first generation of payloads, altitude was determined from an onboard barometer. The equipment rose through the atmosphere and was carried away with the wind, without any possible way to assess the wind profile. Later versions of the equipment used a light that could be followed using a theodolite for the first few kilometers, allowing wind profile measurements. It was possible to obtain a full profile by employing a radar. More recently, Béland & Brown (1988a and 1988b) developed another payload.

Here we describe our technology, strongly inspired from the later work, but with some improvements that appear to be decisive in the comprehension of the physical process that generates optical turbulence. Section 2 gives the principles and few basics of turbulence theory, and § 3 presents a technical description. A discussion of potential errors or misinterpretations is detailed in § 4, followed by astronomical applications in § 5, ending with the conclusion in § 6.

2. PRINCIPLE AND BRIEF THEORETICAL REVIEW

Assuming that the air temperature is a passive and conservative scaling quantity additive and that dynamical atmospheric turbulence follows a Kolmogorov (1941) behavior, Obukhov (1949) and Yaglom (1949) deduced that the structure function of the temperature (T) field (in fact, it would be more precise to say the potential temperature field, which takes into account

that pressure decreases with height) is given by

$$D_T(r) = C_T^2 r^{2/3} \quad \text{for} \quad l \ll r \ll L, \tag{1}$$

where the structure function is $D_T(r) = \langle [T(x) - T(x+r)]^2 \rangle$, $\langle \ldots \rangle$ denotes an ensemble average, and r is the separation between the two sensors.

This equation indicates that the variance of temperature difference scales with a 2/3 power law (which depends on the behavior of Kolmogorov law) and is proportional to the strength of the temperature turbulence C_T^2 in a given region, the distance r being greater than the inner scale l and lower than the outer scale L. For r of the order of or larger than the outer scale, the structure function saturates toward an asymptotic value. At this stage, the existence of metric or decametric outer scale in our atmosphere (i.e., of the order of magnitude of the diameter of large telescope) will affect any interpretation of adaptive optics or interferometric observations.

There is a straightforward relationship between the temperature and the refractive index structure constants C_T^2 and C_N^2 at each altitude h, taking into account the Gladstone formula

$$C_N^2(h) = C_T^2(h) \left[\frac{80.10^{-6} P(h)}{T(h)^2} \right]^2, \tag{2}$$

where P is the pressure (hPa) and T is the absolute temperature (K).

Since it is not possible to make an ensemble average, we assume the temporal stationarity of the process and compute the average for the temporal series. But it is well known that stationarity does not apply for most meteorological phenomena, and some *local* statistical homogeneity is supposed. Any astronomer knows that seeing varies from minute to minute, from night to night, and so on.

3. TECHNICAL DESCRIPTION

As done by Bufton et al. (1972), the variance of the temperature fluctuations is computed onboard. Every 1.4 s a $D_T(h)$ is passed to an off-the-shelf Vaisala meteorological sonde that sends to the ground not only the optical turbulence readings, but also meteorological parameters such as pressure, relative humidity, absolute temperature, and sonde position (Omega and now GPS network) with time.

The data elaborated inside the payload are transmitted to a sophisticated receiver, a Digicora station from Vaisala, which sorts, visualizes, and sends the measurements to a computer to record them.

3.1. Sensors

A 5 μm wide, 60 mm long wolfram wire is used as thermal probe. The resistivity is 220 Ω at 20°C, and the resistivity thermal coefficient $\alpha \sim 3.5 \times 10^{-3}$ K^{-1}. The wire is folded around seven small metallic pins (0.1 mm in diameter) so as to fit inside an 8 mm cube. The current inside the wire is 1 mA. The voltage sensitivity is 730×10^{-6} V K^{-1}, and the cutoff frequency is 320 Hz for a relative wind speed of 4 m s^{-1}.

Several pairs of sensors (two to four) can be present on the same payload. Various separations r between sensors can be set before a given flight, allowing us to assess several estimations of the structure function $D_T(r)$.

3.2. Electronic Diagram

As seen in Figure 1, each pair of sensors is placed in a Wheatstone bridge. Voltages are amplified, processed, digitized, and sent to the ground through a frequency modulation. Two to four pairs can be processed simultaneously.

Before launch, the sensors are encapsulated in an isothermal box, and the bridge is balanced with an adjustable resistor in such a way that any differential voltage will be proportional to the difference in temperature between the two sensors.

In order to avoid very low frequency drift due to the amplifiers, a 0.3 Hz high-pass filter is applied before the onboard computation of $D_T(r)$ is performed. The energy contained within this low-band frequency is also transmitted to the ground. The voltage relevant to a given sensor is low-pass filtered, giving an extra assessment of the temperature, and is sent to the ground. It will then be possible to compare it to the same measurement made with the normal Vaisala sonde.

In sum, a set of eight parameters is sent to the ground through a multiplexer: $D_T(r_1)$, $D_T(r_2)$, the respective energies in the 0–0.3 Hz band for both distances, the absolute temperature T of the ambient air, the internal temperature of the sonde, and two reference voltages.

3.3. Payload Assembly

Figure 2 shows our payload, ready to fly.

3.4. Performance

Instrument performance relies on the type of wire utilized, the off-the-shelf meteorological sonde, the positioning system, and the ascent speed. Here we discuss the performance of the most recent technology we used; i.e., a 5 μm wolfram wire and an RS80-15E Vaisala sonde with GPS and a vertical speed of $\sim$4 m s^{-1}.

Scientific Parameters

1. The $D_T(r)$ noise threshold is about 1.4×10^{-8} K^2 for all altitudes. For the various altitudes of 1, 3, 10, and 20 km, the corresponding $C_N^2(r)$ for $r = 1$ m are, respectively, 1.0, 0.7, 0.25, and 0.1×10^{-20} m$^{-2/3}$, according to equation (2). With two sensors 30 cm apart and for a layer of 6 m thickness, about 20 fluctuation periods are sampled, so the relative error of the signal dispersion estimate is expected to be 20%–25%. Electronic gain and offset are set up during fabrication.

2. Pressure P is given with a precision of 0.5 hPa.

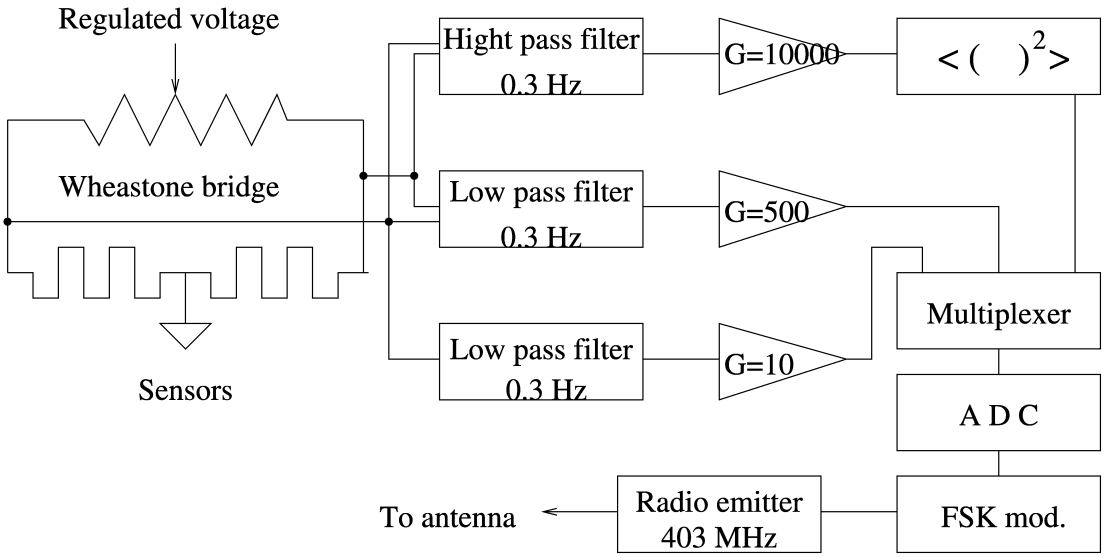

FIG. 1.—Schematic diagram of onboard electronics used to compute $D_T(r)$.

3. Temperature T_{Vaisala} is given with a precision of 0.2 K by the Vaisala sensor. One of our sensors is also fed to an amplifier to give the absolute air temperature T_{Azouit}. Once the flight is completed, this signal is calibrated by comparison with T_{Vaisala}, giving us the true α coefficient of the wire.

4. Relative humidity Rh is given with a precision of 1%.

5. Modulus of wind speed $|\boldsymbol{v}|$ is given with a precision of 0.2 m s^{-1}.

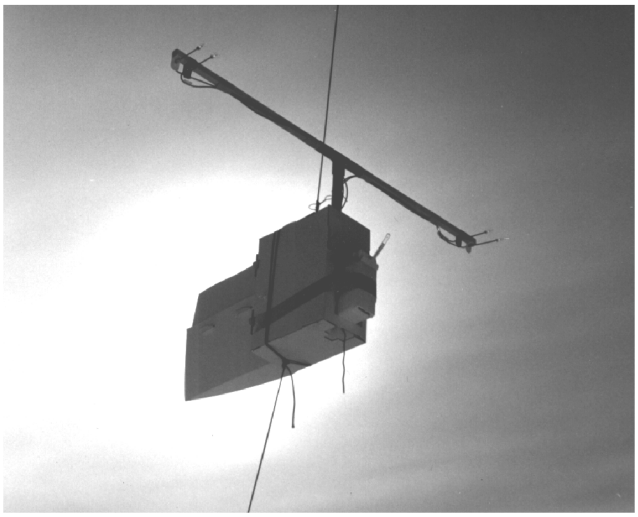

FIG. 2.—Payload in a tethered version. One can see the horizontal wooden arm equipped with two pairs of microthermal sensors about 1 m apart. The electronics are encapsulated in foam to protect them from cold air. On the right, the Vaisala sonde is visible with its humidity/temperature sensor, and below we see the antenna. On the left, a cartoon wing is seen, which forces the payload to stay in front of the relative wind.

6. C_T^2, P, T, and Rh are given every 1.4 s, which corresponds to a 5.6 m vertical resolution.

7. Wind speed and direction are computed and smoothed every 10 s, corresponding to a 40 m vertical resolution.

Experimental Parameters

1. The voltage of the preset equilibrium of the Wheatstone bridge is sent to the ground to check for low-frequency behavior of $T(x) - T(x + r)$, which might also be polluted by very low frequency drift of the amplifiers. This signal has not yet been scientifically used, but the presence of stairlike changes means that the wolfram wire might have slid at one end, abruptly increasing the resistor of one of the two microthermal sensors. When this occurs, it generates an artificial C_N^2 glitch, which can be manually removed. Fortunately, this spurious signal, which appeared very seldom in the past, has been corrected now with technical improvements.

2. A measurement of the internal temperature is also sent to the ground. It is used onboard to regulate the ambient temperature inside the payload, adjusting the dissipation of a resistor. Indeed, the outside air may reach temperatures as low as -70°C, which inhibits the functioning of the electronics. The temperature regulation ensures a normal working environment ($T > 0$°C) and minimizes the voltage drifts.

3. Knowing the altitude of the sonde and the elapsed time after the launching, it is possible to retrieve the ascent speed.

3.5. Versatility

As explained in § 3.2, five channels are available for scientific parameters, such as C_T^2 or the Wheatstone bridge equilibrium. Most of the flights utilize a horizontal arm on which

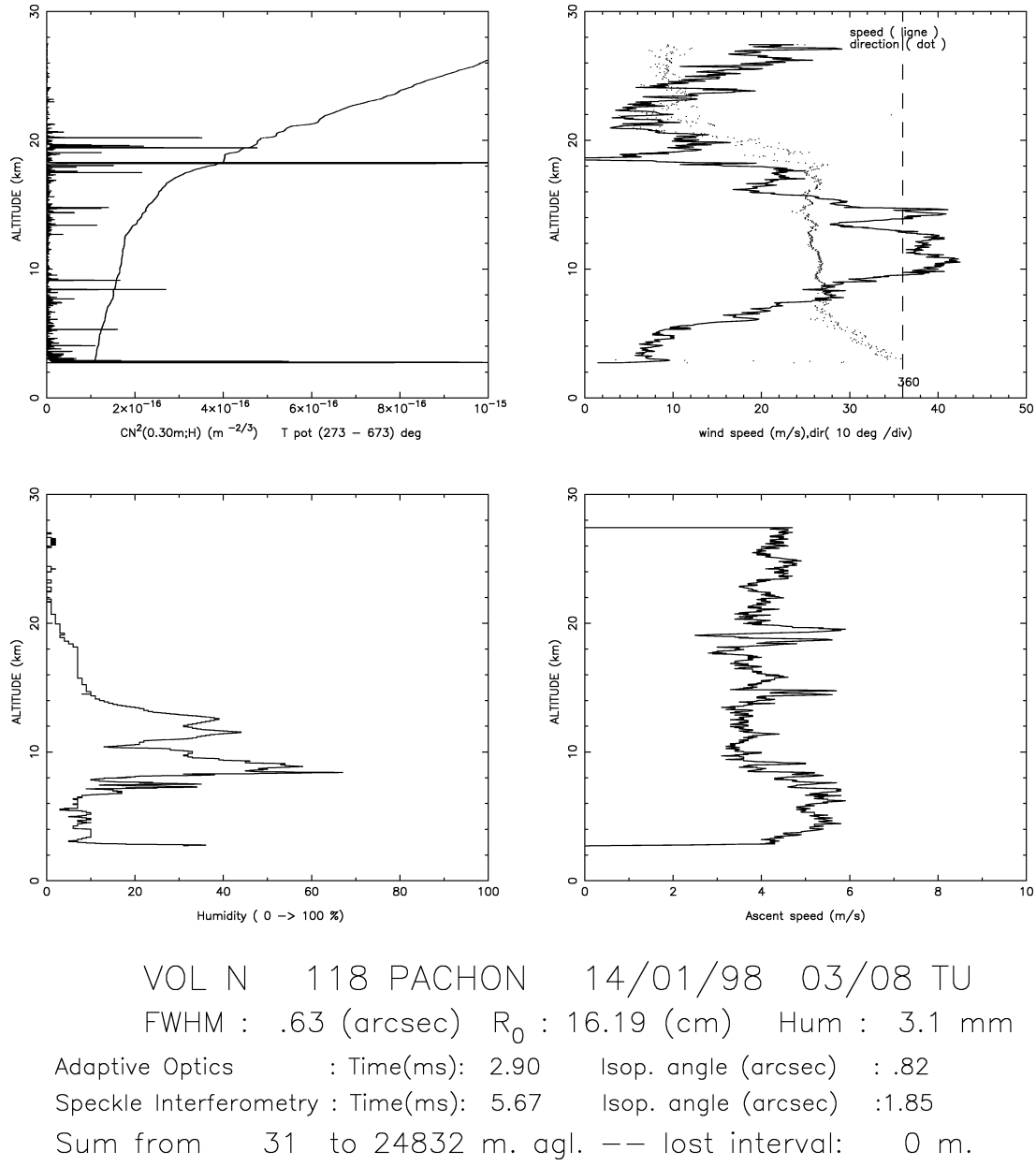

FIG. 3.—Data for flight 118 for 1998 January 14, launched from Cerro Pachón, Chile.

are fixed two pairs of sensors, one 1 m apart and the other 0.3 m apart. It is a convenient method that permits at least one $C_N^2(h)$ profile, even if one microthermal sensor is broken during the launch.

If one is interested in sampling the Kolmogorov spatial spectrum at different distances, it is possible to attach up to four pairs of microthermal sensors, the separation of which could be, for example, 10 cm, 30 cm, 1 m, and 3 m. Given the size of each sensor, a separation of less than 2 cm is impossible, and taking into account the overall weight a meteorological balloon is able to carry, it seems difficult to achieve separations of more than 3 to 4 m. In order to test the isotropy of the Kolmogorov spectrum, it is easy to place a couple of sensors on a horizontal leg and another on a vertical one. These two above mentioned geometries have been tested, but it is not our goal here to comment on the shape of the optical turbulent spectrum.

We also tried a combination of two payloads 100 m apart below the same balloon, each sonde being tuned to a different frequency and using two receiving stations. The launch is somewhat acrobatic, but it worked. From this kind of experiment, one can deduce, or at least have an idea, of the horizontal

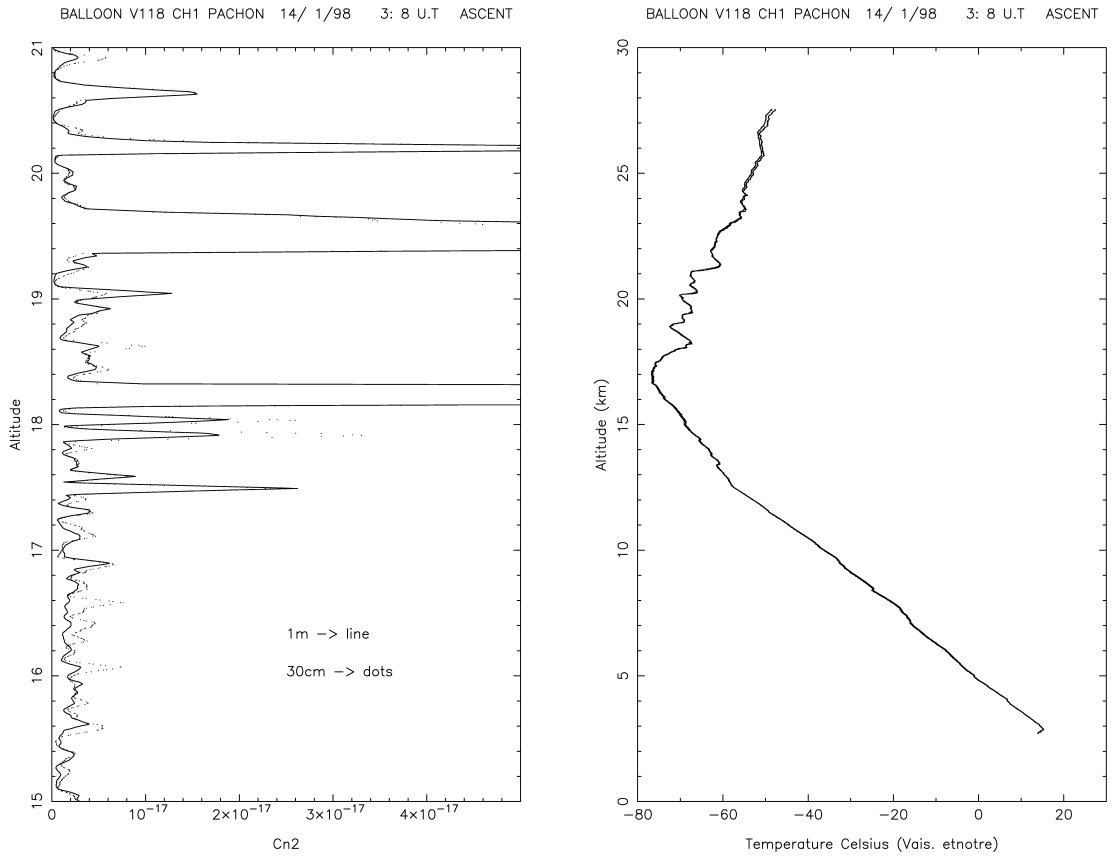

FIG. 4.—*Left*: C_n^2 profiles deduced from two pairs of sensors, one 1 m apart, the other 30 cm apart, between 15 and 21 km. *Right*: $T_{\rm Vaisala}$ and $T_{\rm Azouit}$ temperature profiles (almost no difference).

extent of a turbulent layer, as already noted by Dalaudier et al. (1994), and can verify the presence of stable "sheets" in the atmosphere.

3.6. Example of a Typical Flight

In Figure 3 one can see various vertical profiles. The top left panel plots the turbulence profile $C_N^2(h)$ (close to the left axis) along with a potential temperature (*smooth curve*) deduced from the absolute temperature. The potential temperature takes into account the fact that pressure vanishes with altitude and is expressed as

$$\theta(h) = T(h)\left[\frac{1000}{P(h)}\right]^{0.286}. \quad (3)$$

The vertical gradient of the potential temperature reflects the statical stability of the atmosphere: it is unstable, neutral, or stable when $\delta\theta/\delta h$ is negative, zero, or positive, respectively. From ground level up to 12 km, this gradient is slightly positive and very stable above 17 km. A lot of very thin layers are visible, the two most important being at ground level and 18.2 km.

At top right is shown the vertical wind speed profile, modulus, and direction. The bottom left panel gives a vertical cut of the relative humidity profile. Finally, the bottom right plot gives the ascent speed. From the vertical profile of the relative humidity, one can deduce the water vapor content (here 3.1 mm), which is an important parameter for infrared or millimeter astronomy. At the bottom of Figure 3 are also given the "FWHM seeing," Fried's r_0, and isoplanatic angles.

In Figure 4 at left are plotted two optical turbulence profiles obtained with the sensors at 1 m (*line*) and 30 cm (*dots*) apart, and on the right two temperature profiles given by the Vaisala and our sonde. Note that in a few turbulent layers, $C_N^2|_{30\,\rm cm} > C_N^2|_{1\,\rm m}$. This means that $[D_T(r)/r^{2/3}]|_{30\,\rm cm} > [D_T(r)/r^{2/3}]|_{1\,\rm m}$, as follows from equation (1), and this fact demonstrates that at 1 m, there is already a loss in the expected variance, most likely due to an outer-scale effect.

4. DISCUSSION

4.1. Turbulent Wake of the Balloon

As already noted by Barat et al. (1984), the geometry of the turbulent wake of the balloon has to be taken into account if

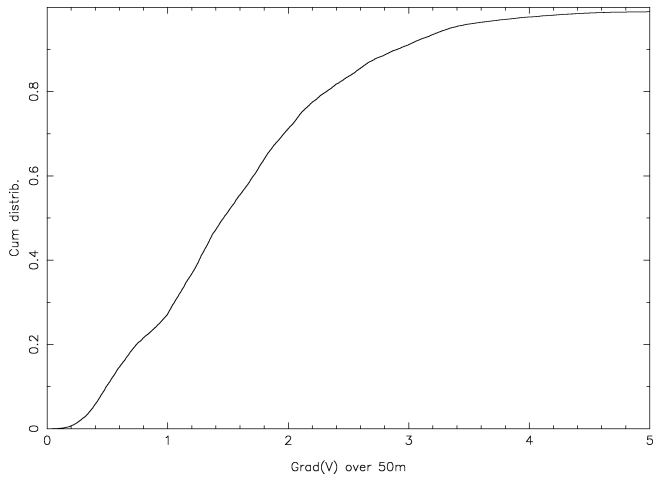

FIG. 5.—Horizontal wind speed gradient cumulative distribution for 20 flights during Gemini site testing campaign and with a 50 m rope between balloon and payload.

one wants to prevent the microthermal sensors from reading this turbulence, which has nothing to do with the real atmospheric turbulence. The diameter of the wake more or less increases linearly until it reaches twice the balloon diameter, and then still increases, but very slowly. Assuming an ascent speed $V_{\rm asc}$, a distance $L_{\rm rope}$ between the balloon and the payload, and a radius $R_{\rm balloon}(h)$, the relative wind between payload and balloon needs to be bound by the following constraint if one wants to avoid the wake:

$$V_{\rm relative} \geq 2R_{\rm balloon}(h)\,\frac{V_{\rm asc}}{L_{\rm rope}}\,. \tag{4}$$

This means that $V_{\rm relative} \geq 0.13(0.32)$ m s^{-1} if $R_{\rm balloon}(h) = 0.8(2)$ m, $L_{\rm rope} = 50$ m, and $V_{\rm asc} = 4$ m s^{-1} for $h = 0(20)$ km.

Figure 5 gives the cumulative distribution of the horizontal wind speed gradient calculated over a distance of 50 m and averaged over about 20 flights during the Cerro Pachón site testing campaign. One can see that a 0.32 m s^{-1} relative wind occurs less than 2% of the time, which is negligible.

4.2. Hot Wire Effect

It is possible that a very high current inside the wire might warm it and initiate a convective effect in which the relative wind removes calories. King's law (1914) relates the thermal heating ΔT of a thread versus the intensity I (in ampere units) and the wind u:

$$\Delta T(I, u) = \frac{I^2}{A + Bu^{1/2}}\,, \tag{5}$$

where A and B are experimental constants (12×10^{-6} and 8×10^{-6}, respectively). For an ascent speed of 4 m s^{-1} and a 1 mA current, the thermal heating is as small as 36×10^{-3} K, and the variability due to differential wind fluctuations Δu between sensors is $2.5 \times 10^{-3}\Delta u$, which is negligible when one recognizes that at 1 m apart, wind fluctuations are of the order of mm s^{-1}.

TABLE 1

GS INTEGRATED VARIABLES COMPARED WITH THE BALLOONS FOR $h > 20$ m FOR EACH RUN AND FOR THE WHOLE GEMINI 1998 CAMPAIGN

	$\langle\varepsilon\rangle$			
RUN DATE	GS	Balloon	$N_{\rm prof.}$ GS	$N_{\rm Flight}$ Balloon
Jan	0.80	0.53	2227	8
Apr	0.76	0.96	399	4
Jul	1.22	0.87	1534	6
Oct	0.72	0.54	2740	7
All	0.85	0.67	6900	25

NOTE.—Average seeing is deduced from $N_{\rm prof.}$ issued by the GS technique or $N_{\rm Flight}$ instrumented balloons.

5. APPLICATIONS

The applications discussed below come from various site testing campaigns that took place at Aire sur l'Adour, Haute Provence Observatory, and Toulouse in France, Cerro Paranal and Cerro Pachón in Chile, Observatorio Roque del los Muchachos in Spain, and finally South Pole, in Antarctica.

The relatively high cost of each balloon, around $1000 (US), means that this technique is more likely to be used for astronomical sites under evaluation, where no optical devices can

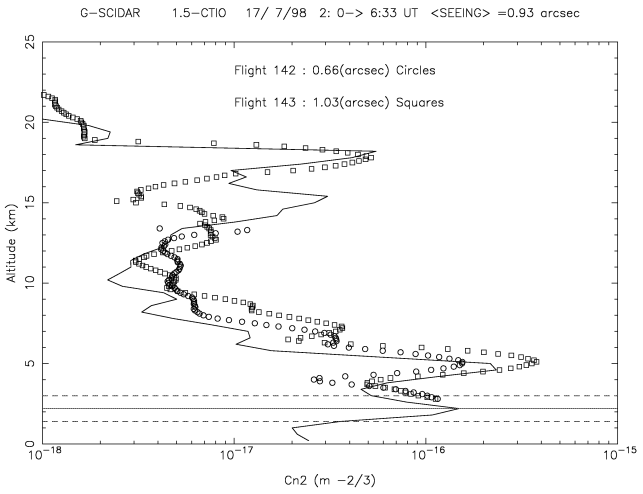

FIG. 6.—Comparison between GS data and that of two balloons launched on 1998 July 17 at Cerro Pachón. The first balloon (Flight 142; *circles*) was launched at 2:02 (UT), and the second (Flight 143; *squares*) at 4:20. Solid line plots the $C_N^2(h)$ profile deduced from the GS during the same period, from 2:00 to 6:33.

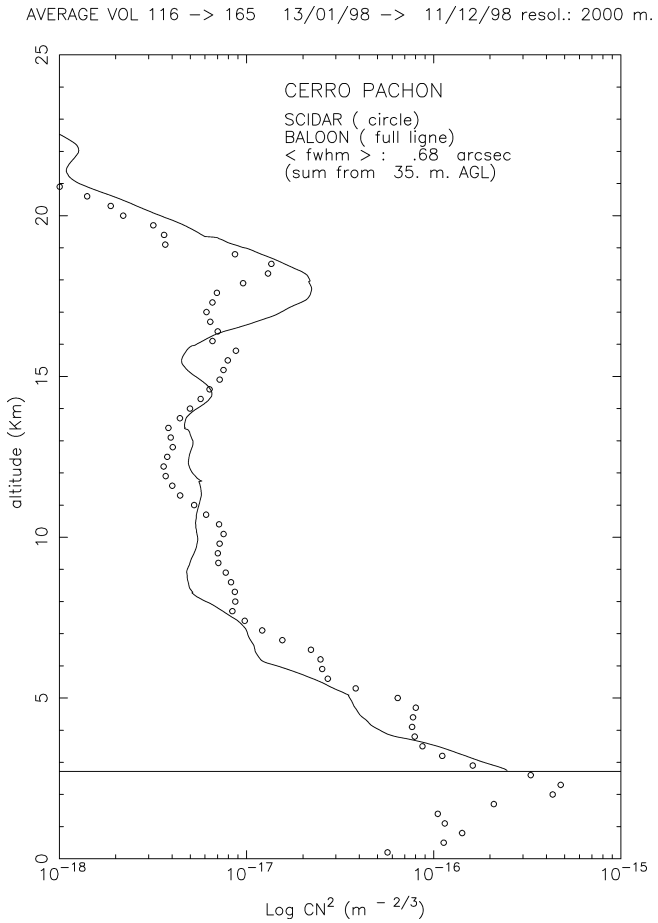

FIG. 7.—Comparison between GS data and that of balloons over the whole year (1998) during the Gemini South site testing campaign.

be installed at the focus of a telescope, or when a high vertical resolution is needed, as is the case in atmospheric physics.

5.1. Atmospheric Physics

Our payload is suitable for atmospheric physics, since it can assess not only the microstructure of the temperature field, but also the macrostructure of T, P, Rh, and wind. With such a set of parameters, we have been able to show that optical turbulence is confined within thin "laminae" (Vernin & Muñoz-Tuñón 1994; Coulman et al. 1995) at the top and the bottom of a thick dynamical turbulent layer. This phenomenon was then confirmed by Werne & Fritts (1999), who simulated a perturbed stable stratified shear flow. This fact helps us to understand why the optical turbulence outer scale is so small (Abahamid et al. 2004a, 2004b).

5.2. Astronomy

Modern techniques in astronomy, such as adaptive optics and interferometry, require a precise and quantitative knowledge of seeing ε, isoplanatic angle θ, coherence time τ, and cone effect d_0. These quantities are related to the vertical profiles of C_N^2 and $V(h)$ above the observatory, along the optical path. The above mentioned quantities are defined within a four-dimensional cube (x, y, z, t), and up to now no experiment exists that is able to assess the optical properties within such a cube. Even GS might give different C_N^2 profiles when exploring different parts of the sky, as discussed by Masciadri et al. (2002). In the case of the balloons, they are dragged away by the wind during their ascent. A typical balloon flight will take 1.5 hr to reach 20 km, an altitude at which the balloon might be 100 km away from its launch pad, depending on the wind speed. This distance is much larger than the 20 km radius of a 45° cone of observation centered around an observatory at 20 km altitude. Nevertheless, a lot of comparisons have been performed in the past with optical devices such as SCIDAR, GS, DIMM, which demonstrate good qualitative and quantitative coherence. This might be explained by (1) the large horizontal extent of the turbulent layers, which fluctuate but remain active over many hours, and (2) the fact that optical turbulence is concentrated within hundreds of thin "laminae" (Coulman et al. 1995), which compensates for the poor accuracy achieved in each layer.

Various publications have shown the good agreement between our in situ balloon turbulence measurements and those taken with optical devices. Bally et al. (1996) measured the seeing with a Hartmann DIMM at South Pole and found good agreement with our integrated C_N^2 profiles (Marks et al. 1999). Avila et al. (1997) gave an example of a good comparison between profiles obtained by one of our balloon and the GS at the Nordic Optical Telescope. In 1998, a 1 yr site testing campaign took place at Cerro Pachón and Cerro Tololo in the framework of the Gemini project, using balloons, GS, DIMM, and GSM techniques (see Avila et al. 2000). Taking into account the fact that the balloons were launched from the Cerro Pachón site (2700 m), which is 500 m above the Cerro Tololo site (2200 m), where the GS was localized, the comparison over 4 weeks is very good, as shown in Table 1. Another example of coherence between balloon and GS data is shown in Figure 6. Figure 7 plots the comparison between balloon and GS measurements over an average of 26 flights. Here again, one can note the quantitative agreement.

5.3. Modeling

From the first flight until now, about 170 launches have been successful. These have produced a large database that allows us to model the behavior of the vertical change in optical turbulence. This database has been processed by Abahamid et al. (2004a) and leads us to propose a model for the behavior of $C_N^2(h)$ and $L_0(h)$ in the boundary layer (first km) and the free atmosphere.

6. CONCLUSION AND PERSPECTIVE

During the last decade, about 170 balloon-borne instruments have been launched successfully from many different sites worldwide. The technology has been improved regularly to reach its present sophisticated state. It is reliable, accurate, and versatile and is easily adaptable to fulfill different goals, such as astronomical site evaluation, new site assessment, atmospheric physics, and modeling. It has been intensively cross-compared with different techniques such as DIMM, generalized SCIDAR, GSM, and masts. It is a very useful device when the site is not accessible to optical instruments that require infrastructure, as in Antarctica. We hope to launch our payloads from Dome C as soon as a permanent base is operational.

We are indebted to many people who helped us to improve our equipment, in particular J. F. Manigault, who developed an incredible skill at passing and attaching a 5 μm thread to the metallic supports of our sensors. We also thank all those who helped us in the delicate launching phase, and the institutes (CNRM and CNES) that kindly let us use their radio receiving station.

REFERENCES

Abahamid, A., Jabiri, A., Vernin, J., Benkhaldoun, Z., Azouit, M., & Agabi, A. 2004a, A&A, 416, 1193
Abahamid, A., Vernin, J., Benkhaldoun, Z., Jabiri, A., Azouit, M., & Agabi, A. 2004b, A&A, 422, 1123
Avila, R., Vernin, J., Chun, M., & Sánchez, L. J. 2000, Proc. SPIE, 2007, 721
Avila, R., Vernin, J., & Masciadri, E. 1997, Appl. Opt., 36,7898
Bally, J., Theil, D., Billawala, Y., Potter, D., Loewenstein, R. F., Mrozek, F., & Lloyd, J. P. 1996, Publ. Astron. Soc. Australia, 13, 22
Barat, J., Cot, C., & Sidi C. 1984, J. Atmos. Oceanic Tech., 1, 270
Barletti, R., Ceppatelli, G., Paternò, L., Righini, A., & Speroni, N. 1976, A&A, 66, 1380
———. 1977, A&A, 54, 649
Bean, B. R., & Dutton, E. J. 1968, Radio Meteorology (New York: Dover)
Béland, R. R., & Brown, J. H. 1988a, Phys. Scr., 37, 419
Brown, J. H., & Béland, R. R. 1988b, Phys. Scr., 37, 424
Bufton, J. L. 1973a, J. Atmos. Sci., 30, 83
———. 1973b, Appl. Opt., 12, 1785
Bufton, J. L., Minott, P. O., Fitzmaurice, M. W., & Titterton, P. J. 1972, J. Opt. Soc. Am., 62, 1068
Coulman, C. E. 1972, Boundary-Layer Meteorology, 4, 169
Coulman, C. E., Vernin, J., & Fuchs, A. 1995, Appl. Opt., 34, 5461
Dalaudier, F., Sidi, C., Crochet, M., & Vernin, J. 1994, J. Atmos. Sci., 51, 237
King, L. V. 1914, Phil. Trans. Roy. Soc. London A, 214, 373
Kolmogorov, A. N. 1941, Dokl. Akad. Nauk SSSR, 30
Marks, R. D., Vernin, J., Azouit, M., Manigault, J. F., & Clevlin, C. 1999, A&AS, 134, 161
Masciadri, E., Avila, M., & Sánchez, L. J. 2002, A&A, 382, 378
Obukhov, A. M. 1949, Izv. Akad. Nauk SSSR, 13
Vernin, J., & Muñoz-Tuñón, C. 1994, A&A, 284, 311
Werne, J., & Fritts, D. C. 1999, Geophys. Res. Lett., 26, 439
Yaglom, A. M. 1949, Dokl. Akad. Nauk SSSR, 69